

Submesoscale Flows Impact Agulhas Leakage in Ocean Simulations

René Schubert^{1,*}, Jonathan Gula^{2,3}, and Arne Biastoch^{1,4}

¹GEOMAR Helmholtz-Centre for Ocean Research Kiel, Kiel, Germany

²Univ Brest, CNRS, IRD, Ifremer, Laboratoire d'Océanographie Physique et Spatiale (LOPS), IUEM, Brest, France

³Institut Universitaire de France (IUF), Paris, France

⁴Christian-Albrechts-University Kiel, Kiel, Germany

*corresponding author, rschubert@geomar.de

Abstract

Agulhas leakage, the warm and salty inflow of Indian Ocean water into the Atlantic Ocean, is of importance for the climate-relevant Atlantic Meridional Overturning Circulation. South of Africa, the eastward turning Agulhas Current sheds Agulhas rings, cyclones and filaments of order 100 km that carry the Indian Ocean water into the Cape Basin and further into the Atlantic. Here we show that the resolution of submesoscale flows of order 10 km in an ocean model leads to 40 % more Agulhas leakage and more realistic Cape Basin water-masses compared to a parallel non-submesoscale resolving simulation. Moreover, we show that submesoscale flows strengthen shear-edge eddies and in consequence lee cyclones at the northern edge of the Agulhas Current, as well as the leakage pathway in the region of the filaments that takes place outside of mesoscale eddies. This indicates that the increase in leakage can be attributed to stronger Agulhas filaments, when submesoscale flows are resolved.

Introduction

Agulhas leakage (AL), the amount of warm and salty Indian Ocean water that enters the Atlantic, is of importance for the Atlantic Meridional Overturning Circulation^{1–4} which impacts the global climate⁵. A prominent contribution to AL is provided by Agulhas rings⁶, which are large mesoscale anticyclones irregularly shed by the retroflecting Agulhas Current (AC). They propagate northwestward through the Cape Basin into the Atlantic carrying the AC water with them. A smaller contribution to AL is provided by cyclonic mesoscale eddies and filaments that form at the northern edge of the AC^{6–9}. In this study, we explore the impact of submesoscale dynamics of $\mathcal{O}(10 \text{ km})$ on the amount and pathways of AL. The strong eddy-eddy interactions in the Cape Basin are associated with the formation of submesoscale vortices along the eddy edges that strengthen the mesoscales^{10,11}, drive a watermass exchange with the surrounding water^{12–15} and thus mix Agulhas ring water out of the rings into the Cape Basin. Submesoscale flows are thus hypothesised to broaden the leakage pathway within the Cape Basin. Upstream, the strong horizontal shears between the AC and the waters on the shelf lead to mesoscale and submesoscale barotropic instabilities^{7,16}. Both instabilities are associated with downstream-propagating meanders and shear-edge eddies that grow in size with time^{7,9,16}. The shear-edge eddies are associated with surface-intensified warm plumes that occasionally propagate onto the shelf^{7,16–18}. Moreover, the shear-edge eddy driven shelf-interior exchange impacts the ecosystems on the shelf, which is of importance for the South African fishery⁷. Submesoscale flows are hypothesised to strengthen the shear-edge eddies and thus to enhance the related shelf-interior exchange and the potentially associated AL. In contrast to the plumes, the shear-edge eddies are trapped between the continental slope and the AC accumulating cyclonic vorticity^{7,18}. The vorticity leaks downstream towards the tip of the Agulhas Bank where it is absorbed by cyclones in the lee of the Agulhas Bank⁹. The lee cyclones can reach diameters of more than 200 km, detach from the slope and propagate southwestward into the Cape Basin, which potentially contributes to AL^{9,12,19}. Moreover, the lee cyclones drive the formation of Agulhas filaments that contribute to AL by transporting AC waters northwestward into the Cape Basin^{7,8,20}. Two Global Drifter Program surface drifter trajectories²¹, from which one is shown in Figure 1, prove that AC waters can leak into the Atlantic by getting trapped in a shear-edge eddy, being transferred to a lee cyclone, leaving the lee cyclone in the Cape Basin and finally reach the Atlantic as part of the Good Hope Jet.

For this study, the effect of submesoscale flows onto AL is isolated by comparing the two numerical ocean simulations INALT60 and INALT20r that have been extensively validated against observations¹⁰. Both are global ocean simulations with a 1/20° grid refinement for the greater Agulhas region and differ only in that INALT60 has a secondary submesoscale-permitting 1/60° grid-refinement for the core Agulhas region ($0^\circ E - 40^\circ E$, $25^\circ S - 45^\circ S$). Besides the smaller horizontal and vertical grid-spacing, the effective dissipation and diffusion are also reduced in the domain of the secondary grid-refinement, contributing further to an increase in the effective resolution²². At around 28°E, the strength, variability, structure and extent of the Agulhas Current has been shown to be similar in both simulations and close to in situ observations¹⁰. This indicates that the secondary grid-refinement has only a small impact on the simulated largescale dynamics of the northern Agulhas Current. In

50 the southern Agulhas Current and the Cape Basin, INALT20r does not simulate submesoscale flows and showed deficiencies in
 51 the representation of in particular cyclonic mesoscales, while INALT60 simulates submesoscale and mesoscale flows, which
 52 compare very well statistically with satellite observations^{10,11}. The presence or absence of submesoscale flows can also be seen
 53 in model snapshots of the surface normalised relative vorticity (Fig. 1).

54
 55 The present study shows that the resolution of submesoscale flows leads to 40 % more Agulhas leakage, more realistic
 56 Cape-Basin water-masses, as well as stronger shear-edge eddies and lee cyclones and a stronger Good Hope Jet. Further, we
 57 show that in particular the leakage pathway outside of mesoscale eddies is stronger when submesoscale flows are resolved and
 58 that it is located in the region of the Agulhas filaments. Combining, our results indicate that submesoscale flows are important
 59 for the formation of Agulhas filaments and the associated leakage.

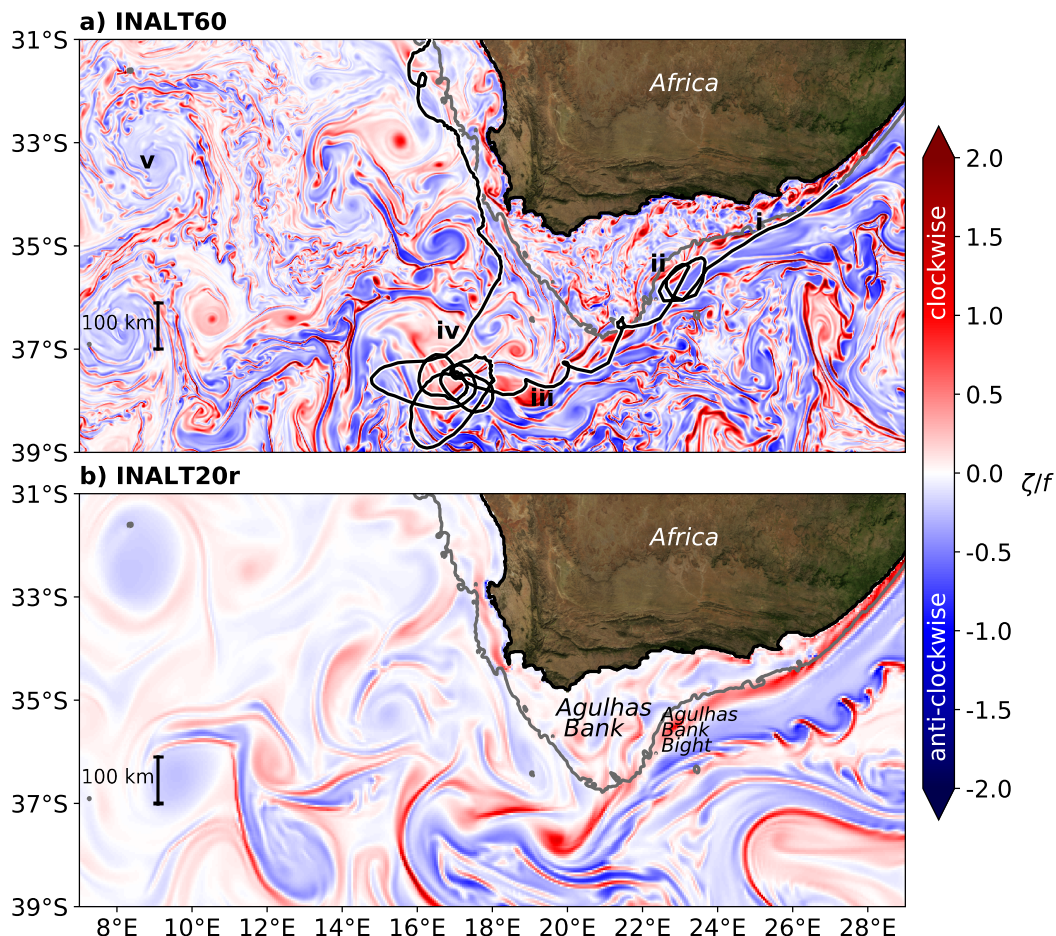


Figure 1. Submesoscale flows in the Agulhas region A zoom into snapshots of surface normalised relative vorticity (a measure of rotation) from INALT60 (a) and INALT20r (b) on model day July 18th 2012. The black-white line shows the trajectory of the Global Drifter Program drifter number 101938 released on Feb 19th 2013. The extent of the Agulhas bank is highlighted with the 300 m isobath. Different dynamical features are marked: i) submesoscale instabilities at the northern edge of the Agulhas Current ii) a shear-edge cyclone in the Agulhas Bank Bight, iii) a shear-edge cyclone southwest of the Agulhas Bank, iv) a lee cyclone, and v) an Agulhas ring with surrounding submesoscale vortices. For land areas a satellite picture is shown²³.

60 Results

61 Agulhas Leakage: Hydrography, Amount and Eddy Sojourn

62 Resolving submesoscale flows leads to a salinification and warming of the water masses that enter the South Atlantic from the
 63 Cape Basin. In the upper 2500 m of the Agulhas ring path, in particular light South Atlantic Central Waters, South Atlantic

64 Subtropical Mode Waters, and Antarctic Intermediate Waters show larger salinities in INALT60 compared to INALT20r (Fig.
65 2a). Moreover, the warmer water masses increase in volume, while the colder decrease in volume, when submesoscale flows
66 are resolved (numbers in Fig. 2a). The salinification and the warming point to a stronger contribution of Indian ocean waters to
67 the Cape Basin water mass properties and thus an increase of Agulhas leakage (AL). Further, a comparison to the reanalysis
68 product GLORYS12V1²⁴ shows that the salinification and the warming improve the realism of the simulation (Fig. 2a). In
69 particular the properties of the light South Atlantic Central Waters, the South Atlantic Subtropical Mode Waters and the
70 Antarctic Intermediate Waters are more realistic when submesoscales are resolved. However, in INALT60 there is too much
71 volume of very light South Atlantic Central Waters ($> 16^{\circ}\text{C}$) compared to the observations.

72 To investigate the AL and its pathways, we use a Lagrangian approach²⁵ that has been established^{2, 26–29}. Virtual particles
73 are released in the simulated AC at 32°S (Fig. 2b, blue line). AL is then computed as the sum of the initial transports of all
74 particles that reach the Good Hope Line west of Africa (Fig. 2b, violet line). Indeed, the mean AL transport increases from
75 8.5 Sv by about 40 % to 12.0 Sv, if submesoscale flows are resolved. The latter is closer to but smaller than the observational
76 estimates of 15 Sv³⁰ and the newer value of 21 Sv³¹, which has however been estimated for a different particle starting section
77 that is known to be associated with higher AL. Note also that in another recent $1/20^{\circ}$ simulation of the Agulhas region a higher
78 average leakage transport of 9.7 Sv is found³². Possible reasons for the difference to the present $1/20^{\circ}$ simulation are (among
79 others) a larger nest domain, a smaller vertical resolution, and a longer integration length.

80 To reveal on which spatial scales and which rotational sense the AL particles move in the Cape Basin, and how this changes
81 when submesoscale flows are resolved, the mean AL transport is shown for both simulations as a function of trajectory curvature
82 scales in Figure 2c. For every trajectory, the distribution of its trajectory curvature scale between 20°E and the Good Hope Line
83 is multiplied by its transport, subsequently summed up over all trajectories and finally normalised by the number of release
84 days. As expected, AL particles are associated more often with curvature scales smaller than 35 km, when submesoscales are
85 resolved. These motions occur both within and outside of mesoscale eddies. For curvature scales larger than 35 km, there is
86 a pronounced increase on the cyclonic side, but only a small increase on the anticyclonic side, in particular for scales larger
87 than 150 km. This indicates that the AL particles sojourn similarly often in anticyclonic mesoscale eddies (> 150 km) in both
88 simulations, but more often in cyclonic mesoscale eddies or outside the mesoscale eddies, when submesoscales are resolved.
89 The integral of the whole distribution gives the mean AL transport. The increase of the total AL transport from INALT20r to
90 INALT60 (3.6 Sv) can be split into an increase due to a 0.5 Sv submesoscale, a 1.1 Sv cyclonic mesoscale, a 0.5 Sv anticyclonic
91 mesoscale and a 1.5 Sv straight contribution. The different contributions are obtained by integrating the difference of the two
92 scale distributions between -35 km and +35 km (submesoscales), +35 km and +400 km (cyclonic mesoscales), -400 km and
93 -35 km (anticyclonic mesoscales) and identifying the difference between the sum of the three integrals and the total AL transport
94 to be the contribution of straight flows. The threshold of 35 km has been chosen, as this is the regional baroclinic Rossby radius
95 of deformation³³, and 400 km as only rarely eddies with larger diameters have been detected in altimetry measurements of the
96 region¹⁰.

97 Here, an eddy detection algorithm³⁴ is applied to investigate, where and how long the AL particles sojourn in cyclones
98 and anticyclones in the Cape Basin, as well as how often they cross the eddy edges. As expected, the exchange through the eddy
99 edges increases when submesoscale flows are resolved. Between 20°E and the Good Hope Line, the average (normalised by
100 the number of seeding days) transport of leakage particles through anticyclonic eddy edges is 100 Sv in INALT20r and 154 Sv
101 in INALT60, and through cyclonic eddy edges it is 61 Sv in INALT20r and 102 Sv in INALT60. Consistently, a much smaller
102 fraction of the AL particles stays most of the travel time (> 90 %) within anticyclones in INALT60 (Fig. 2d). In contrast to the
103 anticyclones, only a very small fraction of AL particles stay longer than 50 % of the time within cyclones in both simulations
104 (Fig. 2d). The percentage of AL particles that stay more than 5 % of the time in cyclones is slightly higher, when submesoscales
105 are resolved.

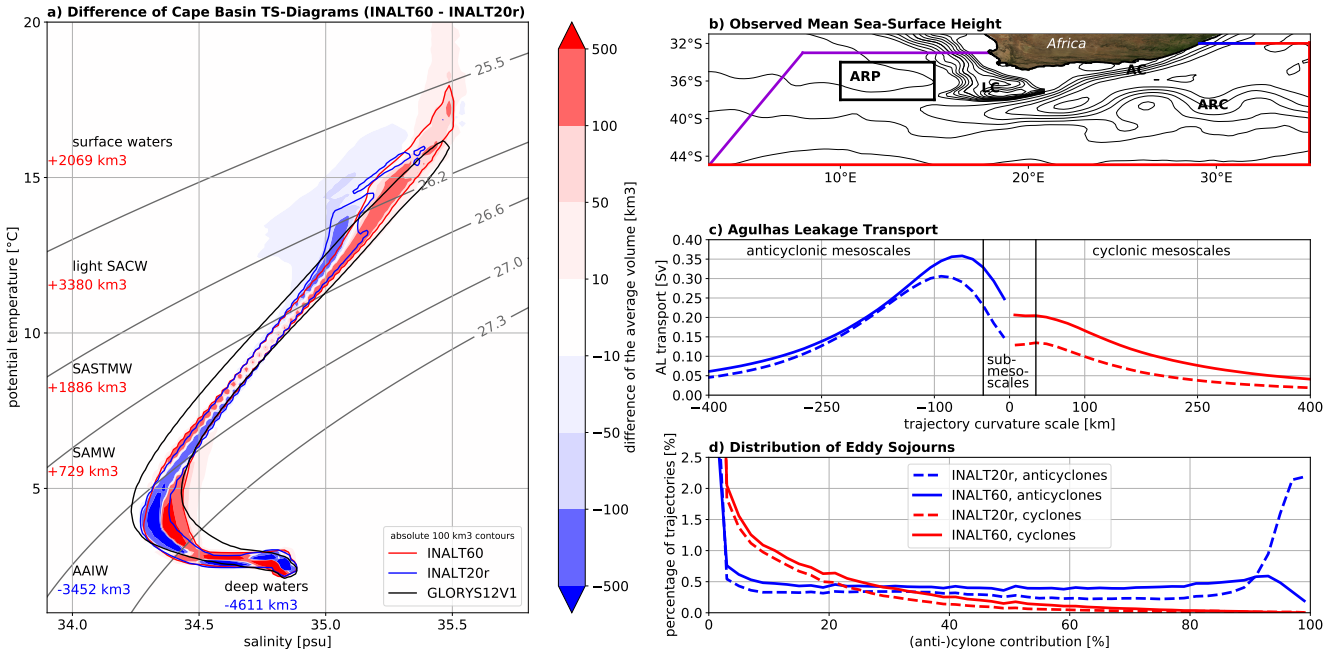


Figure 2. Submesoscale flows salinify the ring path waters, enhance Agulhas leakage, in particular by strengthening non-anticyclonic leakage pathways, and lead to a stronger exchange of Agulhas rings with their surrounding. a) Colours show the difference of INALT60 and INALT20r in the mean water volume associated with specific temperature-salinity properties in the upper 2500 m of the ring path (black box in b)) for the period 2012 - 2017. Red, blue and black lines show the respective absolute 100 km³ contours for INALT60, INALT20r and the reanalysis product GLORYS12V1²⁴. Grey contours show potential density contours that define the water-masses of surface waters, light South Atlantic Central Water (SACW), South Atlantic Subtropical Mode Water (SASTMW), South Atlantic Mode Water (SAMW), Antarctic Intermediate Water (AAIW) and deep waters³⁵. For each water-mass the sum over the difference of the respective volumes is given. b) The 2012-2017 mean sea-surface height from the L4 CMEMS satellite altimetry product with a contour interval of 20 cm and southwest of Africa of 2 cm for the interval -30 cm to -10 cm to highlight the location of the time-mean lee cyclone (LC), the Agulhas Current (AC), the Agulhas Return Current (ARC) and the Agulhas Ring Path (ARP). Virtual Lagrangian particles are seeded within the AC at 32°S (blue) and contribute to Agulhas leakage if they reach the Good Hope Line (violet). The trajectories are also terminated, if they reach the red lines. For land areas a satellite picture is shown²³. c) The average Agulhas leakage transport decomposed into its contributions from trajectory curvature scales between 20°E and the Good Hope Line. d) The distribution of the fraction of (anti-) cyclonic eddy sojourns for the leakage trajectories in the same region. c) and d) join the same legend.

109 Agulhas Leakage Pathways

110 To investigate the submesoscale effect on the respective AL pathways, frequency maps of AL particles are shown for INALT20r
 111 and INALT60 for the full trajectories, as well as for AL particles that sojourn in mesoscale cyclones or anticyclones, and
 112 outside of mesoscale eddies within the Cape Basin (Fig. 3). In INALT20r, the AL pathway is narrow (Fig. 3a). The AL
 113 particles sojourn to a large extent in mesoscale anticyclones, but much less in mesoscale cyclones or outside of mesoscale eddies
 114 (Fig. 3b-3d). If submesoscale flows are resolved, the AL pathway is much broader, in particular northwest of the seamount
 115 chain between the Schmitt-Ott seamount and the Agulhas bank (Fig. 3e). The majority of the AL particles also sojourns in
 116 mesoscale anticyclones, with similar frequencies than in the non-submesoscale resolving experiment but more particles sojourn
 117 in mesoscale cyclones and between the mesoscale eddies (Fig. 3f-3h). Highest cyclonic frequencies are found northwest of the
 118 retroreflection in a band with frequencies decreasing southwestward from a maximum in the lee of the Agulhas bank. The band is
 119 co-located with a minimum in the time-mean sea-surface height (SSH) in the lee of the bank and reduced SSH southwest of it,
 120 attributable to the formation and propagation of lee cyclones. This is not found in INALT20r, which shows that submesoscale
 121 flows strengthen lee cyclones and the related AL. However, the southwestward decreasing frequencies highlight that the AL
 122 particles are mainly mixed out of the lee cyclones and rarely cross the southwestern edge of the ring path within a lee cyclone.
 123 Compared to cyclonic AL frequencies, residual frequencies increase more strongly when submesoscales are resolved (Fig.
 124 3d and 3h). Higher residual frequencies are found in particular between the central ring path and the time-mean lee cyclone:
 125 the region where Agulhas filaments develop. Above the shelf, higher frequencies are found around 34°S in the region of the
 126 Good Hope Jet, which is stronger in INALT60 (identifiable by the distance of the SSH contours in Fig. 3). This may explain
 127 shorter average travel-times of AL particles from the seeding section to the Good Hope Line when submesoscales are resolved
 128 (235 days in INALT60 and 278 days in INALT20r). The drifter pathway shown in Figure 1 is a typical example for a particle
 129 trajectory that reaches the Atlantic with the Good Hope Jet. Our results indicate that the resolution of submesoscale flows
 130 provides a near-shelf fast route into the South Atlantic by strengthening filaments, enhancing the mixing through the Agulhas
 131 ring and lee cyclone edges, as well as by strengthening the Good Hope Jet.

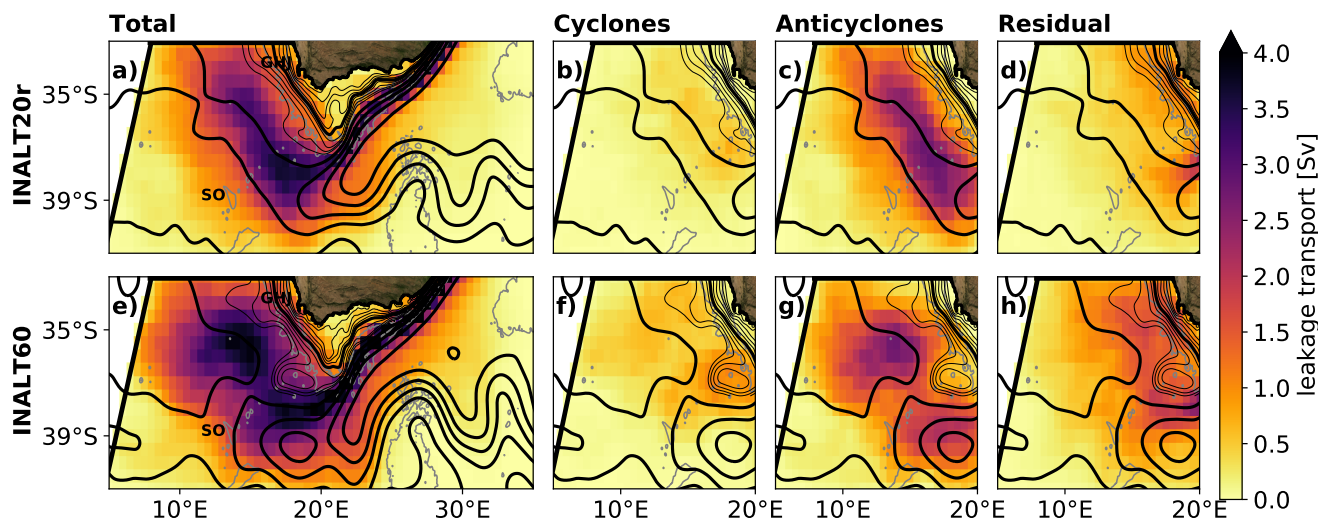


Figure 3. Submesoscale flows broaden the Agulhas leakage pathway and enhance the leakage mainly by leading to a stronger Agulhas filament pathway. Single-count cumulative transport of leakage particles normalised by the number of seeding days (colors) from INALT20r (a-d) and INALT60 (e-h) for the seeding period 2011 - 2014 and the full trajectories (a,e), as well as for leakage particles that sojourn in mesoscale cyclones (b,f), anticyclones (c,g) and outside of mesoscale eddies (d,h) within the Cape Basin. The bin size is $1/2^\circ \times 1/2^\circ$. Black contours show the 2012-2017 mean sea-surface height with contour intervals of 20 cm (thick), as well as of 2 cm between -30 cm and -10 cm north of 37.5°S (thin) to highlight the location and strength of the time-mean lee cyclone and the Good Hope Jet (GHJ). Black straight lines mark the position of the Good Hope Line. Grey contours show 300 m and 3000 m isobaths. The position of the Schmitt-Ott seamount (SO) is marked. For land areas a satellite picture is shown²³.

132 Agulhas Cyclone Formation

133 The presence of the time-mean SSH minimum in and southwest of the lee of the Agulhas bank in INALT60, and its absence
 134 in INALT20r (Fig. 3), show that submesoscale flows strengthen the lee cyclones. Moreover, the time-mean SSH minimum
 135 also exists with a similar amplitude in the mean observed SSH from L4 CMEMS (Fig. 2b) showing that the strengthening
 136 is necessary for a realistic representation of the lee cyclones in the simulation. This contributes to the very good agreement
 137 between INALT60 and observations in terms of scale distribution and numbers of strong cyclones in the Cape Basin, while
 138 INALT20r lacks strong cyclones¹⁰.

139

140 We hypothesise that the strengthening of the lee cyclones, when submesoscale flows are resolved, can be attributed to
 141 the resolution of submesoscale barotropic instabilities at the northern edge of the AC. The resulting eddies have diameters
 142 of about 10 km and grow in size during their downstream propagation^{16,36}. We hypothesise further that the growing features
 143 are dominant drivers of the formation of shear edge eddies, which are downstream dominant drivers of the formation of lee
 144 cyclones. To test both hypotheses, we analyze the surface kinetic energy transfers through spatial and temporal scales when
 145 the AC is not in a strong meandering state (see Methods). At spatial scales of 10 km and 20 km, the energy transfer Π is
 146 mainly directed towards smaller scales (downscale) (Fig. 4a-b). In the open ocean, the downscale transfer is mainly confined
 147 to frontogenetic regions¹¹. Strongest downscale fluxes occur at 10 km, 20 km and 60 km scales in a narrow band along the
 148 northern edge of the AC upstream of its separation from the continental slope (Fig. 4a-c). The narrow band is interrupted in the
 149 Agulhas Bank Bight, where upscale fluxes are found for scales of 20 km and 60 km. In the open ocean, the mean fluxes mainly
 150 change to upscale at scales between 20 km and 60 km. The results indicate that submesoscale instabilities upstream of the
 151 Agulhas Bank Bight extract kinetic energy from the AC and transfer it to scales smaller than 10 km. The resulting features
 152 grow in size and feed their kinetic energy upscale into the shear-edge eddies, in particular into the ones trapped in the Agulhas
 153 Bank Bight. Features that leak from the Agulhas Bank Bight are observed to accelerate and to be squeezed south of the tip of
 154 the Agulhas Bank⁹. This squeezing contributes to the downscale transfer found for the region downstream of the Agulhas Bank
 155 Bight. Further, the leaking features are occasionally small compared to the trapped shear-edge eddies⁹. The separation of the
 156 small features from the shear-edge eddy might provide a further contribution to the downscale transfer. Finally, a maximum of
 157 the upscale transfer through scales of 60 km southwest of the Agulhas Bank shows the strengthening of the lee cyclones by the
 158 absorption of the leaked features.

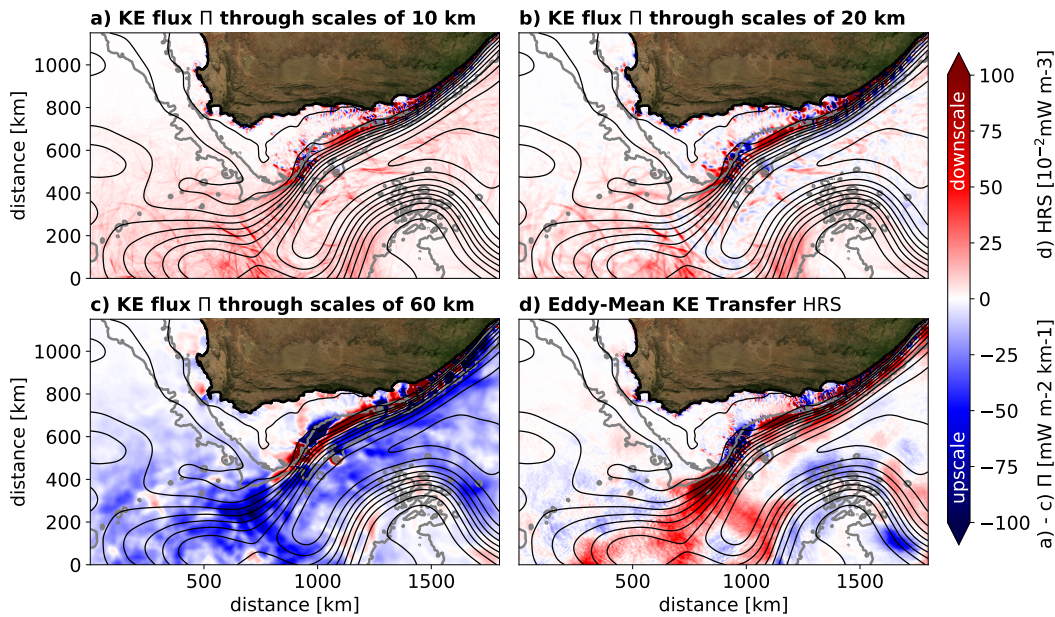


Figure 4. Submesoscale flows strengthen shear-edge eddies and lee cyclones. The mean surface kinetic energy flux Π through horizontal scales of (a) 10 km, (b) 20 km, and (c) 60 km, as well as the mean surface eddy-mean kinetic energy transfer HRS (d) in INALT60. The quantities are computed based on 4-hour mean output and averaged over periods when the Agulhas Current is not in a strong meandering state for the period 2012 - 2017. Negative values show upscale fluxes to larger scales and positive downscale fluxes to smaller scales. Black contours show the 2012 - 2017 mean SSH with an interval of 10 cm and grey contours the 300 m and 3000 m isobaths. For land areas, a satellite picture is shown²³.

159 More evidence that shear edge eddies are mainly driven by submesoscale upscale fluxes instead of large scale barotropic
160 instabilities is achieved by analysing the mean surface kinetic energy transfer from the time-mean to the time-varying flow
161 through horizontal Reynolds stresses (HRS). Positive HRS is a common indicator for barotropic instabilities of a current^{37,38}.
162 The result, shown in Figure 4d, reveals a very narrow band of positive HRS at the northern edge of the AC upstream of the
163 Agulhas Bank Eight. The cross-stream extent of this band (≈ 40 km) gives a scale for the dominant barotropic instability
164 indicating that the AC's northern edge mainly undergoes recurrent submesoscale barotropic instabilities.

165 Conclusion

166 In the present study, we systematically compare a submesoscale-permitting ocean simulations of the Agulhas current system
167 to a parallel simulation that does not resolve submesoscale flows. We show that the resolution of submesoscale flows leads
168 to an increase of Agulhas leakage by 40 % and more realistic Cape-Basin watermasses. Resolving submesoscale barotropic
169 instabilities at the northern edge of the Agulhas Current leads to a strengthening of shear-edge eddies which leads further to a
170 strengthening and thus better representation of lee cyclones west of the Agulhas Bank. However, a Lagrangian analysis indicates
171 that the leakage particles trapped in lee cyclones are mainly mixed out of the eddies within the Cape Basin and only rarely
172 reach the South Atlantic within the southwestward propagating eddies. Instead, leakage particles in the Cape Basin are found to
173 sojourn more often outside of mesoscale eddies and to follow more often straight trajectory segments. As the leakage particles
174 outside of eddies are found mainly in the region of the Agulhas filament development, we conclude that submesoscales enhance
175 the leakage mainly by leading to stronger filaments, as a result of the stronger lee cyclones. Leakage particles also sojourn
176 more often outside of mesoscale eddies as a direct effect of submesoscale instabilities along the eddy edges, which enhance the
177 exchange of eddy waters with their surrounding. Moreover, leakage particles are more often found in the region of the Good
178 Hope Jet that is stronger when submesoscale flows are resolved. The latter might be attributable to a better resolved bathymetry.
179 Remarkably, leakage particles are rarely found to sojourn on the shelf of the Agulhas bank east of $20^{\circ}E$ in both simulations
180 (Fig. 3a). This indicates that warm plumes moving onto the shelf, that should be better represented when submesoscales are
181 resolved, do not play a role for the leakage. A limitation of the study is the eddy detection method that only detects larger
182 eddies with a pronounced SSH signature and that assumes vertical eddy edges. Future research should focus on the vertical
183 structure of Cape Basin eddies, submesoscale flows and Agulhas leakage, as well as on the role of smaller mesoscale eddies and
184 small-scale topographic features in the leakage dynamics. For example, the effect of small-scale topography on the splitting
185 of Agulhas rings and its consequences for the Agulhas leakage should be investigated. While we do not expect an effect on
186 the total amount of Agulhas leakage, we expect an effect on the leakage pathways. A further limitation of the study is that
187 submesoscale processes are only partially resolved by the model. Future model simulations and observations with a higher
188 capability of resolving submesoscale flows can shed light on the impact of even smaller scale flows onto the Agulhas leakage.
189 As the Agulhas Leakage is of importance for the climate-relevant Atlantic Meridional Overturning Circulation, the present
190 study indicates that submesoscale flows in the Agulhas region are important for the global climate. In the future, the respective
191 effects could be identified with longer submesoscale resolving simulations that are currently not feasible. Subsequently, a
192 parameterisation of these effects need to be developed for climate models, as even the latest eddy-active $1/4^{\circ}$ CMIP6 climate
193 models do not resolve submesoscale Agulhas dynamics at all.

194 Methods

195 The Model Experiments

196 The two numerical model experiments, analysed for this study, are validated against observations and described in detail in Ref.
197 11. Here, only a short summary is provided. Both ocean-only configurations use a global $1/4^\circ$ grid and a grid refinement down
198 to a $1/20^\circ$ grid-spacing that extends from $50^\circ S, 20^\circ W$ to $6^\circ S, 70^\circ W$ and covers the eastern half of the South Atlantic Ocean
199 and the western half of the South Indian Ocean. Both experiments are initialised with fields from the last time-step of a 30 year
200 spin-up from 1980 - 2009 that has been integrated with this nested configuration under COREv2 forcing³⁹ using 46 vertical
201 z-levels. In contrast, the two simulations here use JRA55-do v1.3 forcing⁴⁰, which is associated with higher temporal and
202 spatial resolution, and 120 vertical z-levels. The simulations are integrated till the end of 2017. The first experiment, performed
203 with the above described configuration, is referred to INALT20r.L120.HighDiff¹⁰. The abbreviation denotes that the model
204 configuration is part of the INALT family²⁹, the horizontal resolution of the nest with the highest resolution (20 for $1/20^\circ$), that
205 a reduced nested domain is used (r), the number of vertical levels (L120) and the diffusion and dissipation setting (explicit
206 diffusion and dissipation and TVD/EEN discretisation schemes (HighDiff) or no explicit diffusion and dissipation and UBS
207 schemes (LowDiff). In this study it is named for simplicity INALT20r. INALT20r resolves almost no submesoscales in the
208 Agulhas region. The second parallel experiment, INALT60.L120.LowDiff (short INALT60), is associated with exactly the same
209 configuration, but with a secondary nest for the core Agulhas region ($45^\circ S, 0^\circ W$ to $25^\circ S, 40^\circ W$) down to a $1/60^\circ$ grid-spacing.
210 Within the second nest, INALT60 resolves a large portion of the submesoscale spectrum and compares well to observations at
211 all simulated scales¹⁰.

212 Normalised Relative Vorticity

213 The normalised relative vorticity is given by ζ/f , where $\zeta = v_x - u_y$ is the vertical component of the relative vorticity (with the
214 zonal velocity component u , the meridional velocity component v , the zonal Cartesian axis x and the meridional axis y) and
215 $f = 2\Omega \sin(2\pi \frac{\theta}{360^\circ})$ is the planetary vorticity (with the angular speed of the Earth $\Omega = \frac{2\pi}{86400}$ s-1 and the latitude θ). Partial
216 derivatives of a with respect to b are written throughout this paper as $\frac{\partial a}{\partial b} = a_b$.

217 Mesoscale Eddy Detection

218 For the detection of mesoscale eddies and their edges, an eddy-detection algorithm³⁴ is applied to the temporally detrended
219 and domain-average reduced daily-mean sea-surface height anomalies interpolated onto a $1/4^\circ$ grid for the region $1^\circ E - 25^\circ E$,
220 $26^\circ S - 44^\circ S$. The sea-surface height anomalies are scanned for thresholds between 1 m (-1 m) to -1 m (1 m) with an increment
221 of 1 cm. If a connected set of 8-1000 pixels with sea-surface height anomalies below (above) the current threshold has a local
222 minimum (maximum) with an amplitude of at least 1 cm, as well as a maximum pixel distance of 700 km, the pixel set is
223 identified to be a cyclone (anticyclone) and its interior pixels are removed from the further detection.

224 Lagrangian Particle Tracking for the Computation of Agulhas Leakage

225 Every model day, virtual particles are released in the simulated AC at a 300-km-long section at $32^\circ S$ (Fig. 1, inlay, blue line)
226 with ARIANE²⁵. At the centre of each vertical grid-cell, one particle is released at 12 AM. The current transport through the
227 respective grid cell is tagged to each particle, while the particles follow the daily 4D daily-mean flow field. If the current
228 transport through a grid-cell exceeds 0.01 Sv, the grid-cell is divided into four similar sized sub-cells and two times four
229 particles are released at the centres of the sub-cells at 6 AM and 6 PM (each associated with 1/8 of the total transport). If the
230 particles reach the Good Hope Line within 3 years, the respective trajectories are terminated and their transports contribute to
231 AL. Trajectories are further terminated, if they reach the boundaries at $45^\circ S, 35^\circ E$ or $32^\circ S$. For this study, particles that are
232 released in the years 2011 - 2014 are analysed.

233 Trajectory Curvature Scale

234 The curvature of a trajectory is given by $\kappa = (x'y'' - x''y')/(x'^2 + y'^2)^{\frac{3}{2}}$ ¹², where x and y are the Cartesian coordinates of
235 the particle positions. Dashes mark temporal derivatives. The Cartesian distance for the derivatives is computed using the
236 Haversine formula. The reciprocal of the curvature is the curvature radius $r = 1/\kappa$. The curvature scale is defined to be the
237 respective diameter, with the opposite sign ($-2r$). A positive (negative) curvature scale corresponds to a cyclonic (anticyclonic)
238 movement.

239 Identifying Periods When the Agulhas Current is Not in a Strong Meandering State

240 Downstream-propagating large meanders of the AC develop in the Natal Bight and are thus referred to as Natal Pulses⁴¹.
241 Natal Pulses occasionally trigger the shedding of Agulhas rings and disturb the evolution of the shear-edge, as well as lee
242 cyclones^{9,42,43}. Here, Natal Pulses are identified at around $28^\circ E$ along the Agulhas Current Timeseries (ACT) section⁴⁴ based
243 on a common methodology⁴⁵ as events, where the offshore-distance of the maximum of the vertically integrated southwestward

cross-section transport is more than one standard deviation larger than average. To account for the variability regarding the short time-scales, which is stronger in INALT60 compared to INALT20r, a further condition is added on the duration of the event. Here, periods with Natal Pulses at the ACT section are identified as periods, when the offshore-distance of the maximum of the southwestward vertical integrated cross-section transport exceeds the average i) for more than 15 consecutive days and ii) by one standard deviation for at least one day of this period. The identified periods agree with those identified by eye in animations of the SSH. Events that fulfil only the second condition are not attributable to Natal Pulses. Based on the SSH evolution along the northern edge of the AC, it is further identified that Natal Pulses need on average about 100 days from the ACT section to the retroflection. Thus, we define Natal Pulse periods as 100 day periods starting with the detection of a Natal Pulse at the ACT section. Besides the Natal Pulses, also other events can strongly disturb the AC in the region of the shear-edge eddy formation. In INALT60, at the end of the model year 2013, a cyclone detached from the ARC's first meander trough, travelled northwestward and lead to a substantial meandering of the southern AC between December 22nd 2013 and February 11th 2014. In this period, the AC is also considered to be in a strong meandering state.

256 Kinetic Energy Transfer Through Temporal and Spatial Scales

The kinetic energy transfer from the time-mean flow to the time-varying flow by horizontal Reynolds stresses is computed as HRS = $-\rho_0[\overline{u' u' \bar{u}_x} + \overline{u' v' (\bar{u}_y + \bar{v}_x)} + \overline{v' v' \bar{v}_y}]^{37,38}$, where $\rho_0 = 1024 \text{ kg m}^{-3}$ is the reference density. Overbars denote the mean over the investigated period and dashes deviations from that mean. Positive HRS is an indicator of barotropic instability^{38,46}. The kinetic energy flux (the rate of kinetic energy transfer) from currents with spatial scales larger than a specific scale L to currents with scales smaller than L is computed as $\Pi = -\rho_0[(\overline{u^2} - \overline{\bar{u}^2})\bar{u}_x + (\overline{u\bar{v}} - \overline{\bar{u}\bar{v}})(\bar{u}_y + \bar{v}_x) + (\overline{v^2} - \overline{\bar{v}^2})\bar{v}_y]^{47-49}$, where the overbars denote convoluted fields using an area-normalised two-dimensional top-hat convolution kernel of diameter L . The definition of the scale kinetic energy flux, in distinction to the spatial transfer of kinetic energy, is associated with a gauge freedom⁵⁰. Here, we use a separation of transfers across scales and in space that has been suggested to be a suitable one due to its Galilean invariance⁵⁰. Details on the application of this method to the INALT60 output are described by Ref. 11. The respective code is available on GitHub⁵¹.

267 Data Availability Statement

This study bases on ocean model output data from two simulations that are described in detail in the literature including the model input data^{10,29}. The size of the model output data is too large for an upload. The data to reproduce the plots of this study can be accessed with the following link:

<https://hdl.handle.net/20.500.12085/c572cde8-a82c-4c2d-9bd7-288dfc8f1939>.

The trajectory of the drifter shown in Figure 1 can be accessed here: <https://www.aoml.noaa.gov/phod/gdp/data.php>. The black contour line in Fig 2a has been computed using E.U. Copernicus Marine Service Information. The respective GLORYS12V1 data can be downloaded here: https://resources.marine.copernicus.eu/?option=com_csw&view=details&product_id=GLOBAL_REANALYSIS_PHY_001_030. The sea-surface height data used for Figure 2b can be accessed here: https://resources.marine.copernicus.eu/?option=com_csw&view=details&product_id=SEALEVEL_GLO_PHY_L4 REP_OBSERVATIONS_008_047.

278 Code Availability Statement

The code to reproduce the figures of this study is provided in the jupyter notebook produce_plots.ipynb (<https://hdl.handle.net/20.500.12085/c572cde8-a82c-4c2d-9bd7-288dfc8f1939>). The code to compute the scale kinetic energy flux using coarse-graining is available at <http://doi.org/10.5281/zenodo.4476094>.

282 Competing Interests Statement

283 The authors declare no competing interests.

284 Author Contributions

285 R.S. and A.B. designed the study and the experimental strategy. R.S. performed the numerical model simulations, developed
286 and executed the analyses, produced all figures and wrote the text. A.B. and J.G. contributed to the analysis, the discussion of
287 the results, and the writing of the manuscript.

288 References

- 289 1. Weijer, W., de Ruijter, W. P., Sterl, A. & Drijfhout, S. S. Response of the Atlantic overturning circulation to South Atlantic
290 sources of buoyancy. *Glob. Planet. Chang.* **34**, 293–311 (2002).

- 291 2. Biastoch, A., Böning, C. W. & Lutjeharms, J. Agulhas leakage dynamics affects decadal variability in Atlantic overturning
292 circulation. *Nature* **456**, 489 (2008).
- 293 3. Biastoch, A. *et al.* Atlantic multi-decadal oscillation covaries with Agulhas leakage. *Nat. Commun.* **6**, 10082 (2015).
- 294 4. Lübecke, J. F., Durgadoo, J. V. & Biastoch, A. Contribution of increased Agulhas leakage to tropical Atlantic warming. *J.*
295 *Clim.* **28**, 9697–9706 (2015).
- 296 5. Zhang, R. *et al.* A review of the role of the Atlantic meridional overturning circulation in Atlantic multidecadal variability
297 and associated climate impacts. *Rev. Geophys.* **57**, 316–375 (2019).
- 298 6. De Ruijter, W. *et al.* Indian-Atlantic interocean exchange: Dynamics, estimation and impact. *J. Geophys. Res. Ocean.* **104**,
299 20885–20910 (1999).
- 300 7. Lutjeharms, J., Catzel, R. & Valentine, H. Eddies and other boundary phenomena of the Agulhas Current. *Cont. Shelf Res.*
301 **9**, 597–616 (1989).
- 302 8. Lutjeharms, J. & Cooper, J. Interbasin leakage through Agulhas Current filaments. *Deep. Sea Res. Part I: Oceanogr. Res.*
303 *Pap.* **43**, 213–238 (1996).
- 304 9. Lutjeharms, J., Boebel, O. & Rossby, H. Agulhas cyclones. *Deep. Sea Res. Part II: Top. Stud. Oceanogr.* **50**, 13–34 (2003).
- 305 10. Schubert, R., Schwarzkopf, F. U., Baschek, B. & Biastoch, A. Submesoscale impacts on mesoscale Agulhas dynamics. *J.*
306 *Adv. Model. Earth Syst.* **11**, 2745–2767 (2019).
- 307 11. Schubert, R., Gula, J., Greatbatch, R. J., Baschek, B. & Biastoch, A. The submesoscale kinetic energy cascade: Mesoscale
308 absorption of submesoscale mixed layer eddies and frontal downscale fluxes. *J. Phys. Oceanogr.* **50**, 2573–2589 (2020).
- 309 12. Boebel, O. *et al.* The Cape Cauldron: a regime of turbulent inter-ocean exchange. *Deep. Sea Res. Part II: Top. Stud.*
310 *Oceanogr.* **50**, 57–86 (2003).
- 311 13. Van Aken, H. *et al.* Observations of a young Agulhas ring, Astrid, during MARE in March 2000. *Deep. Sea Res. Part II:*
312 *Top. Stud. Oceanogr.* **50**, 167–195 (2003).
- 313 14. Capuano, T. A., Speich, S., Carton, X. & Blanke, B. Mesoscale and submesoscale processes in the Southeast Atlantic and
314 their impact on the regional thermohaline structure. *J. Geophys. Res. Ocean.* **123**, 1937–1961 (2018).
- 315 15. Sinha, A., Balwada, D., Tarshish, N. & Abernathey, R. Modulation of Lateral Transport by Submesoscale Flows and
316 Inertia-Gravity Waves. *J. Adv. Model. Earth Syst.* **11**, 1039–1065 (2019).
- 317 16. Tedesco, P., Gula, J., Ménesguen, C., Penven, P. & Krug, M. Generation of submesoscale frontal eddies in the Agulhas
318 Current. *J. Geophys. Res. Ocean.* (2019).
- 319 17. Schumann, E. & van Heerden, I. L. Observations of agulhas current frontal features south of africa, october 1983. *Deep.*
320 *Sea Res. Part A. Oceanogr. Res. Pap.* **35**, 1355–1362 (1988).
- 321 18. Lutjeharms, J., Penven, P. & Roy, C. Modelling the shear edge eddies of the southern Agulhas Current. *Cont. Shelf Res.* **23**,
322 1099–1115 (2003).
- 323 19. Penven, P., Lutjeharms, J., Marchesiello, P., Roy, C. & Weeks, S. Generation of cyclonic eddies by the Agulhas Current in
324 the lee of the Agulhas Bank. *Geophys. Res. Lett.* **28**, 1055–1058 (2001).
- 325 20. Whittle, C., Lutjeharms, J., Rae, D. & Shillington, F. Interaction of Agulhas filaments with mesoscale turbulence: a case
326 study. *South Afr. J. Sci.* **104**, 135–139 (2008).
- 327 21. Malan, N. The Impact of Agulhas Current Dynamics on Shelf Waters: A modelling approach (2017).
- 328 22. Soufflet, Y. *et al.* On effective resolution in ocean models. *Ocean. Model.* **98**, 36–50 (2016).
- 329 23. Stöckli, R., Vermote, E., Saleous, N., Simmon, R. & Herring, D. The Blue Marble Next Generation-A true color earth
330 dataset including seasonal dynamics from MODIS. *Publ. by NASA Earth Obs.* (2005).
- 331 24. Global Monitoring and Forecasting Center (2018). GLORYS12V1 - Global Ocean Physical Reanalysis Product, E.U.
332 Copernicus Marine Service Information [Data set]. Available at https://resources.marine.copernicus.eu/?option=com_csw&view=details&product_id=GLOBAL_REANALYSIS_PHY_001_030 (Accessed: 10th June 2021).
- 333 25. Blanke, B. & Raynaud, S. Kinematics of the Pacific equatorial undercurrent: An Eulerian and Lagrangian approach from
334 GCM results. *J. Phys. Oceanogr.* **27**, 1038–1053 (1997).
- 335 26. Speich, S., Blanke, B. & Madec, G. Warm and cold water routes of an OGCM thermohaline conveyor belt. *Geophys.*
336 *research letters* **28**, 311–314 (2001).

- 338 27. Durgadoo, J. V., Loveday, B. R., Reason, C. J., Penven, P. & Biastoch, A. Agulhas leakage predominantly responds to the
339 Southern Hemisphere westerlies. *J. Phys. Oceanogr.* **43**, 2113–2131 (2013).
- 340 28. Wagner, P., Rühs, S., Schwarzkopf, F. U., Koszalka, I. M. & Biastoch, A. Can Lagrangian tracking simulate tracer
341 spreading in a high-resolution Ocean General Circulation Model? *J. Phys. Oceanogr.* **49**, 1141–1157 (2019).
- 342 29. Schwarzkopf, F. U. *et al.* The INALT family—a set of high-resolution nests for the Agulhas Current system within global
343 NEMO ocean/sea-ice configurations. *Geosci. Model. Dev.* **12**, 3329–3355 (2019).
- 344 30. Richardson, P. L. Agulhas leakage into the Atlantic estimated with subsurface floats and surface drifters. *Deep. Sea Res.*
345 *Part I: Oceanogr. Res. Pap.* **54**, 1361–1389 (2007).
- 346 31. Daher, H., Beal, L. M. & Schwarzkopf, F. U. A new improved estimation of Agulhas leakage using observations and
347 simulations of Lagrangian floats and drifters. *J. Geophys. Res. Ocean.* **125**, e2019JC015753 (2020).
- 348 32. Schmidt, C., Schwarzkopf, F. U., Rühs, S. & Biastoch, A. Characteristics and robustness of agulhas leakage estimates: an
349 inter-comparison study of lagrangian methods. *Ocean. Sci.* **17**, 1067–1080 (2021).
- 350 33. Chelton, D. B., Deszoeke, R. A., Schlax, M. G., El Naggar, K. & Siwertz, N. Geographical variability of the first baroclinic
351 Rossby radius of deformation. *J. Phys. Oceanogr.* **28**, 433–460 (1998).
- 352 34. Chelton, D. B., Schlax, M. G. & Samelson, R. M. Global observations of nonlinear mesoscale eddies. *Prog. Oceanogr.* **91**,
353 167–216 (2011).
- 354 35. Donners, J., Drijfhout, S. & Hazeleger, W. Water mass transformation and subduction in the South Atlantic. *J. physical*
355 *oceanography* **35**, 1841–1860 (2005).
- 356 36. Krug, M., Swart, S. & Gula, J. Submesoscale cyclones in the Agulhas current. *Geophys. Res. Lett.* **44**, 346–354 (2017).
- 357 37. Harrison, D. & Robinson, A. Energy analysis of open regions of turbulent flows—Mean eddy energetics of a numerical
358 ocean circulation experiment. *Dyn. Atmospheres Ocean.* **2**, 185–211 (1978).
- 359 38. Storch, J.-S. v. *et al.* An estimate of the Lorenz energy cycle for the world ocean based on the STORM/NCEP simulation.
360 *J. Phys. Oceanogr.* **42**, 2185–2205 (2012).
- 361 39. Griffies, S. M. *et al.* Coordinated ocean-ice reference experiments (COREs). *Ocean. modelling* **26**, 1–46 (2009).
- 362 40. Tsujino, H. *et al.* JRA-55 based surface dataset for driving ocean–sea-ice models (JRA55-do). *Ocean. Model.* **130**, 79–139
363 (2018).
- 364 41. Lutjeharms, J. & Roberts, H. The Natal pulse: An extreme transient on the Agulhas Current. *J. Geophys. Res. Ocean.* **93**,
365 631–645 (1988).
- 366 42. de Ruijter, W. P., Van Leeuwen, P. J. & Lutjeharms, J. R. Generation and evolution of Natal Pulses: solitary meanders in
367 the Agulhas Current. *J. Phys. Oceanogr.* **29**, 3043–3055 (1999).
- 368 43. van Leeuwen, P. J., de Ruijter, W. P. & Lutjeharms, J. R. Natal pulses and the formation of Agulhas rings. *J. Geophys. Res.*
369 *Ocean.* **105**, 6425–6436 (2000).
- 370 44. Beal, L. M., Elipot, S., Houk, A. & Leber, G. M. Capturing the transport variability of a western boundary jet: Results
371 from the Agulhas Current Time-Series Experiment (ACT). *J. Phys. Oceanogr.* **45**, 1302–1324 (2015).
- 372 45. Krug, M., Tournadre, J. & Dufois, F. Interactions between the agulhas current and the eastern margin of the agulhas bank.
373 *Cont. Shelf Res.* **81**, 67–79 (2014).
- 374 46. Gula, J., Molemaker, M. J. & McWilliams, J. C. Topographic generation of submesoscale centrifugal instability and energy
375 dissipation. *Nat. Commun.* **7**, 12811 (2016).
- 376 47. Leonard, A. Energy cascade in large-eddy simulations of turbulent fluid flows. In *Advances in geophysics*, vol. 18, 237–248
377 (Elsevier, 1975).
- 378 48. Germano, M. Turbulence: the filtering approach. *J. Fluid Mech.* **238**, 325–336 (1992).
- 379 49. Eyink, G. L. Locality of turbulent cascades. *Phys. D: Nonlinear Phenom.* **207**, 91–116 (2005).
- 380 50. Aluie, H., Hecht, M. & Vallis, G. K. Mapping the energy cascade in the North Atlantic Ocean: the coarse-graining
381 approach. *J. Phys. Oceanogr.* **48**, 225–244 (2018).
- 382 51. Schubert, R. & Rath, W. *reneschubert/keflux*: Computing the oceanic kinetic energy flux across spatial scales using
383 coarse-graining (Version v1.0.0). *Zenodo*, <http://doi.org/10.5281/zenodo.4476094> (2021).

384 **Acknowledgements**

385 The model simulations and the data analysis for this study have been executed on high-performance computers of the North
386 German Supercomputing Alliance (HLRN). J.G. gratefully acknowledges support from the French National Agency for
387 Research (ANR) through the projects DEEPER (ANR-19-CE01-0002-01) and ISblue “Interdisciplinary graduate school for the
388 blue planet” (ANR-17-EURE-0015).

389 **List of Figures**

- 390 1 **Submesoscale flows in the Agulhas region** A zoom into snapshots of surface normalised relative vorticity (a
391 measure of rotation) from INALT60 (a) and INALT20r (b) on model day July 18th 2012. The black-white line
392 shows the trajectory of the Global Drifter Program drifter number 101938 released on Feb 19th 2013. The
393 extent of the Agulhas bank is highlighted with the 300 m isobath. Different dynamical features are marked: i)
394 submesoscale instabilities at the northern edge of the Agulhas Current ii) a shear-edge cyclone in the Agulhas
395 Bank Bight, iii) a shear-edge cyclone southwest of the Agulhas Bank, iv) a lee cyclone, and v) an Agulhas ring
396 with surrounding submesoscale vortices. For land areas a satellite picture is shown²³. 2
- 397 2 **Submesoscale flows salinify the ring path waters, enhance Agulhas leakage, in particular by strength-
398 ening non-anticyclonic leakage pathways, and lead to a stronger exchange of Agulhas rings with their
399 surrounding.** a) Colours show the difference of INALT60 and INALT20r in the mean water volume associated
400 with specific temperature-salinity properties in the upper 2500 m of the ring path (black box in b)) for the period
401 2012 - 2017. Red, blue and black lines show the respective absolute 100 km³ contours for INALT60, INALT20r
402 and the reanalysis product GLORYS12V1²⁴. Grey contours show potential density contours that define the
403 water-masses of surface waters, light South Atlantic Central Water (SACW), South Atlantic Subtropical Mode
404 Water (SASTMW), South Atlantic Mode Water (SAMW), Antarctic Intermediate Water (AAIW) and deep
405 waters³⁵. For each water-mass the sum over the difference of the respective volumes is given. b) The 2012-2017
406 mean sea-surface height from the L4 CMEMS satellite altimetry product with a contour interval of 20 cm and
407 southwest of Africa of 2 cm for the interval -30 cm to -10 cm to highlight the location of the time-mean lee
408 cyclone (LC), the Agulhas Current (AC), the Agulhas Return Current (ARC) and the Agulhas Ring Path (ARP).
409 Virtual Lagrangian particles are seeded within the AC at 32°S (blue) and contribute to Agulhas leakage if they
410 reach the Good Hope Line (violet). The trajectories are also terminated, if they reach the red lines. For land
411 areas a satellite picture is shown²³. c) The average Agulhas leakage transport decomposed into its contributions
412 from trajectory curvature scales between 20°E and the Good Hope Line. d) The distribution of the fraction of
413 (anti-) cyclonic eddy sojourns for the leakage trajectories in the same region. c) and d) join the same legend. 4
- 414 3 **Submesoscale flows broaden the Agulhas leakage pathway and enhance the leakage mainly by leading
415 to a stronger Agulhas filament pathway.** Single-count cumulative transport of leakage particles normalised
416 by the number of seeding days (colors) from INALT20r (a-d) and INALT60 (e-h) for the seeding period 2011 -
417 2014 and the full trajectories (a,e), as well as for leakage particles that sojourn in mesoscale cyclones (b,f),
418 anticyclones (c,g) and outside of mesoscale eddies (d,h) within the Cape Basin. The bin size is 1/2° × 1/2°.
419 Black contours show the 2012-2017 mean sea-surface height with contour intervals of 20 cm (thick), as well
420 as of 2 cm between -30 cm and -10 cm north of 37.5°S (thin) to highlight the location and strength of the
421 time-mean lee cyclone and the Good Hope Jet (GHJ). Black straight lines mark the position of the Good Hope
422 Line. Grey contours show 300 m and 3000 m isobaths. The position of the Schmitt-Ott seamount (SO) is
423 marked. For land areas a satellite picture is shown²³. 5
- 424 4 **Submesoscale flows strengthen shear-edge eddies and lee cyclones.** The mean surface kinetic energy flux
425 Π through horizontal scales of (a) 10 km, (b) 20 km, and (c) 60 km, as well as the mean surface eddy-mean
426 kinetic energy transfer HRS (d) in INALT60. The quantities are computed based on 4-hour mean output and
427 averaged over periods when the Agulhas Current is not in a strong meandering state for the period 2012 - 2017.
428 Negative values show upscale fluxes to larger scales and positive downscale fluxes to smaller scales. Black
429 contours show the 2012 - 2017 mean SSH with an interval of 10 cm and grey contours the 300 m and 3000 m
430 isobaths. For land areas, a satellite picture is shown²³. 6